

## Observation of spin-momentum-layer locking in a centrosymmetric crystal

Ke Zhang,<sup>1†</sup> Shiv Kumar,<sup>2</sup> Eike. F. Schwier,<sup>2</sup> Koji Miyamoto,<sup>2</sup> Taichi Okuda,<sup>2</sup> Kenya Shimada,<sup>2\*</sup>

<sup>1</sup> Graduate school of Science, Hiroshima University, Hiroshima 739-0046, Japan.

<sup>2</sup> Hiroshima Synchrotron Radiation Center, Hiroshima University, Hiroshima 739-0046, Japan.

\*Emails: [kshimada@hiroshima-u.ac.jp](mailto:kshimada@hiroshima-u.ac.jp) (K. S.)

**Keywords:** hidden-spin polarization, spin-momentum-layer locking, centrosymmetric, nonsymmorphic

The spin polarization in nonmagnetic materials is conventionally attributed to the outcome of spin-orbit coupling when the global inversion symmetry is broken. The recently discovered hidden spin polarization indicates that a specific atomic site asymmetry could also induce measurable spin polarization, leading to a paradigm shift in research on centrosymmetric crystals for potential spintronic applications. Here, combining spin- and angle-resolved photoemission spectroscopy and theoretical calculations, we report distinct spin-momentum-layer locking phenomena in a centrosymmetric, layered material, BiOI. The measured spin is highly polarized along the Brillouin zone boundary, while the same effect almost vanishes around the zone center due to its nonsymmorphic crystal structure. Our work not only demonstrates the existence of hidden spin polarization, but also uncovers the microscopic mechanism of spin, momentum, and layer locking to each other.

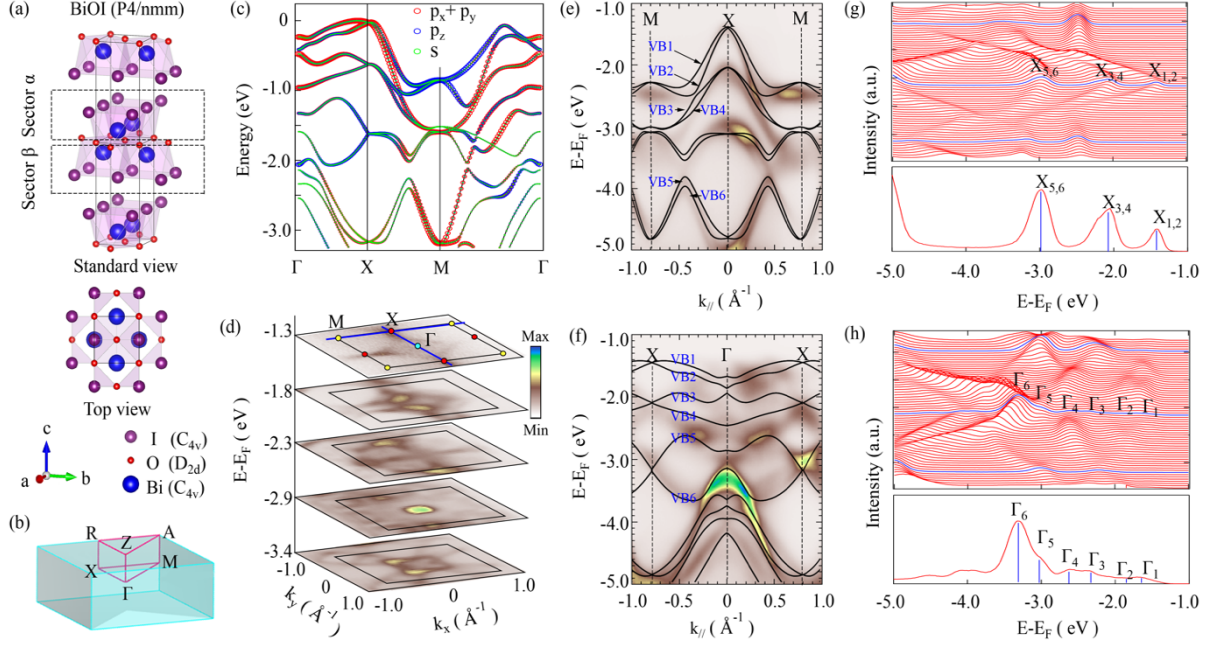
BiOI has a tetragonal crystal structure with a centrosymmetric space group P4/nmm containing nonsymmorphic operations of a glide mirror  $\{M_z | (\frac{1}{2}, \frac{1}{2}, 0)\}$  and two screw axes  $\{C_{2x} | (\frac{1}{2}, 0, 0)\}$ ,  $\{C_{2y} | (0, \frac{1}{2}, 0)\}$ . The inversion center is located in the middle of two inequivalent O atoms (site point group  $D_{2d}$ ), while the Bi and I atoms occupy the noncentrosymmetric polar sites with the site point group  $C_{4v}$ . The polyhedrons coordinated by Bi and I atoms are intersected by the O plane. Hence, the quasi-2D unit cell is divided into two sectors  $\alpha$  and  $\beta$ , respectively, as shown in Fig. 1(a).

The BZ and DFT-calculated electronic structures of BiOI with SOC are shown in Fig. 1(b) and 1(c). The valence band maximum (VBM) is close to the X point. It is noticeable that at the points X and M, the glide reflection symmetry  $\{M_z | (\frac{1}{2}, \frac{1}{2}, 0)\}$  anticommutes with the inversion operator, leading to an extra two-fold degeneracy between two pairs of Kramer's degeneracy, i.e., four-fold degeneracy including the spin. Such a four-fold degeneracy is maintained along the entire X-M line in the absence of SOC. Thus, the band splitting along the X-M line shown in Fig. 1(c) is caused by SOC solely. In analogy to the conventional Rashba/Dresselhaus effect, such a splitting is composed of two sets of spin splitting bands originating from the sectors  $\alpha$  and  $\beta$ , respectively [1]. In comparison, the splitting along the  $\Gamma$ -X line is contributed by both of orbital repulsions and the SOC effect, and is thus larger than that along the X-M line. The orbital projection analysis shows that in the vicinity of the points  $\Gamma$  and X, the top two valence bands (designated as VB1 and VB2) are mainly composed of the  $p_x + p_y$  and  $s$  orbitals, while VB3-VB6 are dominated by the  $p_z$  and  $s$  orbitals.

The ARPES results measured at a photon energy of 65 eV are shown in Fig. 1(d) [constant energy contours (CECs)], Fig. 1(e), 1(f) (band dispersions) and Fig. 1(g), 1(h) [energy-distribution curves (EDCs)]. A square-like CEC exists at  $-1.3$  eV, with corners located at X points. As the energy decreases, the CEC features at the X point expand and eventually form contours surrounding the M point, merging with those centered at the  $\Gamma$  point. This hole-like behavior is presented in the ARPES spectra along the M-X-M line in Fig. 1(e). From the CECs and spectra results, we have found that the VBM is located around the bulk X point,  $\sim 1.4$  eV below the experimental Fermi level.

By directly comparing the calculated bulk band structure with the ARPES data shown in Fig. 1(e) and 1(f), a good agreement is found, indicating that the surface effect that breaks the global inversion symmetry is relatively weak. The predicted four-fold degeneracy at the X and M points and the splitting two-fold

degenerate branches (VB1 to VB6) away from X and M are all supported by the ARPES measured dispersion. Furthermore, Fig. 1(g) and 1(h) show the EDCs measured along the M-X-M and X- $\Gamma$ -X directions. At the X point, the degenerate peaks, *i.e.*,  $X_{1,2}$ ,  $X_{3,4}$  and  $X_{5,6}$  are unambiguously present, while at the  $\Gamma$  point, each of the degenerate peak splits into two individual peaks, *i.e.*,  $\Gamma_1$  to  $\Gamma_6$ . Consequently, three pairs of Rashba-like hole-type valence bands are formed at the X and M points, with the band crossing points located around  $-1.4$  eV,  $-2.1$  eV, and  $-3.0$  eV for the X point, respectively (Fig. 1(e)). These results agree well with our calculation, thus confirming the nonsymmorphic feature of the material.



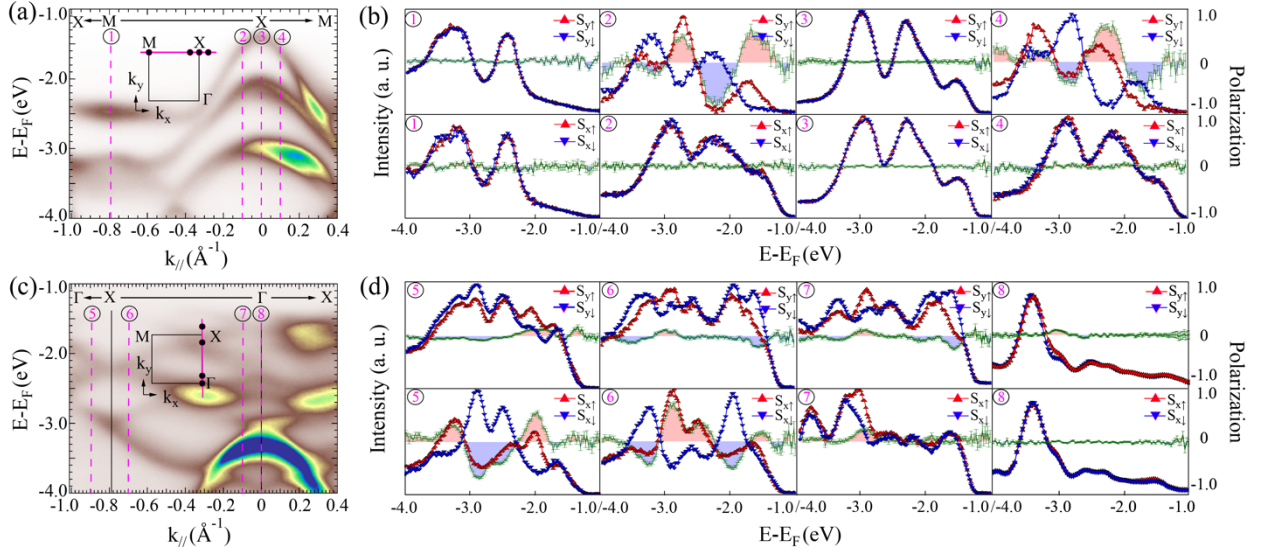
**FIGURE 1.** (a) The crystal structure of BiOI. The unit cell consists of two BiI layers as inversion partners, labelled as a sector  $\alpha$  and  $\beta$ . (b) The bulk Brillouin zone. (c) DFT-calculated bulk band dispersion with orbital projection. (d) ARPES-measured CECs of the valence bands at different energies. (e, f) ARPES-measured spectra along the X-M, and  $\Gamma$ -X high symmetry lines, overlaid by DFT calculated dispersions (solid black lines). (g, h) EDCs corresponding to the spectra shown in (e) and (f), respectively. The lower parts are the EDCs at X and  $\Gamma$  points, respectively, from which one can resolve the spectral peaks corresponding to the top six valence bands.

Figure 2 presents the in-plane spin polarization of BiOI measured by spin-ARPES using photon energies of 65 eV for panels (a, b) and 30 eV for panels (c, d). The wide-ranging measurements involving different photon energies and geometries verified that we have essentially observed the spin polarization and spin textures derived from the initial state. The representative spin EDCs for the three pairs of two-fold degenerate bands VB1-VB6 are shown in Fig. 2(b) and 2(d), with the upper (lower) row showing the spin-resolved EDCs and the corresponding  $S_y$  ( $S_x$ ) spin component. At three time-reversal invariant points M, X and  $\Gamma$  (momentum points ①, ③ and ⑧), the spin-resolved EDCs overlap, indicating negligible spin polarization; this is consistent with the spin degeneracy originating from Kramer's pairs.

When the momenta moved away from the X point, we have observed significant spin polarization (up to 80%) along both  $k_x$  and  $k_y$  directions (momentum points ②, ④, ⑤ and ⑥). For momenta ⑤ and ⑥, nearly all the six VBs were resolved as the individual polarizations peaked with opposing polarization signs in each pair. This is because the band splitting along  $\Gamma$ -X direction was more significant compared to the splitting along the X-M direction (Fig. 1(c), 1(e), 1(f)). In sharp contrast, the spin polarization surrounding the  $\Gamma$  point was very weak ( $<30\%$  for momentum point ⑦), along both  $k_x$  and  $k_y$  directions.

The detected photoemission signal mainly arises from the topmost sector ( $\alpha$ ) of the cleaved BiOI single crystal, which is favourable to detect the spin polarization from a local sector. Compared with the previous measurements of HSP materials such as WSe<sub>2</sub> [3], PtSe<sub>2</sub> [4], LaO<sub>0.55</sub>F<sub>0.45</sub>BiS<sub>2</sub> [5] and Bi2212 [6] that focus on the spin-momentum locking around a single high-symmetry point, our work revealed the distinct polarization features surrounding different high-symmetry points, *i.e.*, BZ center ( $\Gamma$ ) and BZ boundary (X), and observed a sharp contrast between them. Such observations suggest that momentum-dependent spin polarization originates from the HSP rather than merely from the surface potential gradient; further, these observations suggest the key factors affecting the HSP effect, such as the nonsymmorphic symmetry and

orbital characters.



**FIGURE 2.** (a), (c) Band dispersion along M-X and  $\Gamma$ -X directions, respectively. The inset shows the BZ, with black dots indicating the momentum positions where the spin-resolved EDCs are measured. (b), (d) Spin-resolved EDCs and spin polarizations. Each panel's number corresponds to the momentum point denoted by the pink dashed lines in (a), (c). The green error bars indicate the statistical fluctuation in determining the spin polarizations (proportion  $1/\sqrt{N}$ ; where N is the photoemission intensity).

In summary, combining spin-ARPES measurements and theoretical calculations, we report distinct spin-momentum-layer locking phenomena at different BZ positions in a centrosymmetric material BiOI. The measured spin polarization localized on a specific BiI layer is highly polarized along the BZ boundary but almost vanishes around the zone center due to its nonsymmorphic crystal structure. The layer-resolved spin texture, either Rashba or Dresselhaus type, reflects the symmetry of both real space and  $k$ -space. Our findings experimentally demonstrate the existence of the HSP effect and shed light on the design metrics to utilize high spin polarization in centrosymmetric materials by revealing the intimate interplay between spin, orbital, and layer degrees of freedom.

## REFERENCES

2. Zhang YJ, *et al. Chin Phys Lett* **37**, 087105 (2020).
3. Riley JM, *et al. Nat Phys* **10**, 835-839 (2014).
4. Yao W, *et al. Nat Commun* **8**, 14216 (2017).
5. Wu SL, *et al. Nat Commun* **8**, 1919 (2017).
6. Gotlieb K, *et al. Science* **362**, 1271 (2018).
7. Zhang XW, *et al. Nat Phys* **10**, 387-393 (2014).